Chemical Engineering Communications

ISSN: 0098-6445 (Print) 1563-5201 (Online) Journal homepage: www.tandfonline.com/journals/gcec20

Enhanced performance of organic solar cells using silver-sulfide/reduced-graphene-oxide nanocomposite in photoactive and hole-transport layers

Oyugi N. Robert, Tabitha A. Amollo, Kallen M. Nalyanya, Ndiritu J. Maina & Vincent O. Nyamori

To cite this article: Oyugi N. Robert, Tabitha A. Amollo, Kallen M. Nalyanya, Ndiritu J. Maina & Vincent O. Nyamori (19 Feb 2026): Enhanced performance of organic solar cells using silver-sulfide/reduced-graphene-oxide nanocomposite in photoactive and hole-transport layers, Chemical Engineering Communications, DOI: 10.1080/00986445.2026.2627898

To link to this article: https://doi.org/10.1080/00986445.2026.2627898

CHEMICAL ENGINEERING COMMUNICATIONS
https://doi.org/10.1080/00986445.2026.2627898

Taylor & Francis
Taylor & Francis Group

Enhanced performance of organic solar cells using silver-sulfide/reduced-graphene-oxide nanocomposite in photoactive and hole-transport layers

Oyugi N. Robert[a], Tabitha A. Amollo[a,b], Kallen M. Nalyanya[a], Ndiritu J. Maina[a], and Vincent O. Nyamori[c]

[a]Faculty of Science, Department of Physics, Egerton University, Egerton, Nakuru, Kenya; [b]University of Pretoria, Hatfield, Pretoria, South Africa; [c]School of Chemistry and Physics, University of KwaZulu-Natal, Westville Campus, Durban, South Africa

ABSTRACT

This study reports the synthesis and application of Ag_2S-rGO nanocomposite to enhance organic solar cells (OSCs). The nanocomposite was used to modify the photoactive and hole transport layers of the OSC. The synthesis was done using the chemical reduction method. Morphological analysis of the Ag_2S-rGO nanocomposite through scanning electron microscopy (SEM) demonstrated the intercalation of rGO sheets within the nanoparticles of Ag_2S during the chemical reduction process, and that Ag_2S had a nanowire shape. X-ray diffraction (XRD) analysis revealed that Ag_2S nanoparticles are of high crystallinity, having a 1.0 Å to 5.2 Å d-spacing range. The nanocomposite exhibited strong optical absorption in the UV region. The surface plasmon resonance effect associated with Ag_2S nanoparticles, crystallinity, and hydrophilicity of the nanocomposite made it suitable for OSC application. Incorporating Ag_2S-rGO into the OSCs' photoactive layer slightly increased the absorption band within the visible region. All the OSCs with modified active layers and HTL exhibited an improved photovoltaic performance. The nanocomposite improved J_{sc} by enhancing charge generation within the photoactive layer, resulting in a subsequent enhancement in PCE of up to 127%. On the other hand, the nanocomposite improved charge collection at the interface, leading to an enhanced PCE of up to 53%.

KEYWORDS

Hole transport layer; optical properties; organic solar cells; photoactive layer; silver sulfide/reduced graphene oxide nanocomposite; structural properties

Introduction

The technology of organic solar cells (OSCs) is cost-effective in solar energy conversion. The dominating solar cells in the market, made of inorganic materials, require complicated, and expensive manufacturing processes (Khalil et al. 2016). The merits of OSCs include low-cost and straightforward fabrication techniques and materials (Dhuriya et al. 2016). Nonetheless, OSC materials are still under development following the low power conversion efficiency (PCE) of the devices. The primary causes of OSCs' low PCE include poor charge mobility (Ray and Alam 2012) and low optical absorption (Mime et al. 2021). Also, the hole transport layer (HTL) of OSCs is commonly made of poly(3,4-ethylene-dioxythiophene): poly(styrene sulfonate) (PEDOT: PSS), which is soluble in water and acidic in nature (He et al. 2012).

The problem of poor charge mobility and light absorption can be solved using nanofilms. Thin films have been shown to scatter the incident light within the solar cells, thereby enhancing photon harvesting and increasing the OSCs' PCE (Ohib et al., n.d.). Nanoparticles with dimensions below 100 nm exhibit unique size-dependent optical and electrical properties that enhance light absorption and charge transport in organic solar cells. Nanoparticles comprise a large material class, such as particulate substances, with dimensions of not more than 100 nm, and these size-specific optical and electrical characteristics amplify light absorption and charge transportation in organic solar cells (Ibrahim et al. 2019). Ag nanoparticles have localized surface plasmon resonance (LSPR) in the visible region and can be used to achieve high optical absorption and light harvesting in photovoltaic devices (Ohib et al., n.d.; Kareem et al.

CONTACT Tabitha A. Amollo tamollo@egerton.ac.ke Egerton University, Faculty of Science, Department of Physics, P.O. Box 536–20115, Egerton, Nakuru, Kenya.

2020; Delgado et al. 2018). The optical response of silver-based nanostructures is sensitive to particle size, shape, surrounding environment, and the distance between particles, which directly dictate the strength of light and matter interactions in photovoltaic and optoelectronic devices (Kareem et al. 2020). Other properties of Ag_2S NPs that make them resonate with the needs of OSCs include a small band gap (between 0.9 and 1.05 eV) (Kumari et al. 2014), a significant coefficient of absorption, a monoclinic crystal structure (Hamed et al. 2020), good chemical stability, and photoconductivity (Delgado et al. 2018). A nanocomposite of silver sulfide (Ag_2S) and reduced graphene oxide (rGO) can further enhance the PCE of OSCs. Ag_2S-rGO multi-layered composite films in a polymer matrix can have a much higher electrical conductivity of up to 210.18 Scm^{-1} at high temperature and a much higher thermoelectric power factor (Wang et al. 2022). This suggests that the Ag_2S-rGO system can have good electrical transport behavior when incorporated into a composite form. Graphene also has broadband absorption, high charge carrier mobility, high transparency, and high specific surface area, all essential for high-efficiency OSCs (Liu et al. 2017).

Graphene oxide (GO) is graphene in its oxidized form and has functional groups of oxygen decorating the C basal planes (Perrozzi et al. 2015). Graphene oxide also has hydroxylic and epoxy oxygen functional groups on the basal planes, with the edges having a carboxylic group (Amollo et al., 2018). rGO is made from GO through a reduction process to restore the sp^2 carbon network and partially recover graphene's electronic properties, like high charge carrier mobility (Sharma et al. 2017; Sun et al. 2022). The implication is that rGO has lower oxygen and higher electronic conductivity content than GO while maintaining unique graphene properties like electrical conductivity and broad surface area. The suitability of rGO for application in OSCs is that it is possible to tune its sizes between a few nm and μm, allowing for the flexibility of the solar cell devices (Sun et al. 2022). The reduction of GO also introduces defect sites, making the rGO more electrically conductive compared to GO, whose electrical conductivity is inferior to that of graphene due to the functional groups of oxygen (Sharma et al. 2017). In this study, silver sulfide-reduced graphene oxide (Ag_2S-rGO) nanocomposite was prepared and utilized in OSCs' photoactive and hole transport layers. It is envisaged that the complementary effect of LSPR of the NPs and the outstanding properties of rGO would suit the nanocomposite for application in OSCs.

Materials and methods

Materials

Polyvinylpyrrolidone (99%), silver nitrate (99.95%), sodium nitrate (>99.0%), graphite powder (99.99%), hydrogen peroxide (3%) (30%), concentrated sulfuric acid (99.999%), sodium sulfide (99.999%), potassium permanganate (>99.0%), and absolute ethanol were purchased from Kobian, Kenya. Lithium fluoride (LiF) (>99.0%), aluminum (Al) rods (99.5%), P3HT (96.3%), PCBM (>99%), PEDOT: PSS (1.4 wt.% solid content), and Unpatterned ITO-coated substrates were purchased from Ossila.

Nanomaterials synthesis

Graphene oxide (GO) synthesis

The synthesis of GO was achieved through the modified Hummers method (Hummers and Offeman 1958). Graphite powder (1 g), concentrated sulfuric acid (50 ml), and sodium nitrate (1 g) were mixed and stirred for 30 min at 0 °C in an ice bath, followed by the addition of potassium permanganate (6 g) gradually for 10 min. Keeping the temperature at 0 °C during oxidant addition helps control exothermal oxidation reaction and prevent runaway temperature rises by suppressing the formation of explosive potassium permanganate intermediates. After complete addition of the oxidant, the mixture was stirred at 35 °C for 3 h to allow complete oxidation. Hydrogen peroxide (3%) (200 ml) was added, and the stirring continued for 30 min at room temperature (Amollo et al., 2018). The resulting solution was washed to a neutral pH using double-distilled water. The GO films were obtained by drying the washed solution in a vacuum oven set at 50 °C.

Synthesis of Ag_2S NPs and Ag_2S-rGO nanocomposite

The synthesis of Ag_2S followed the protocol of Hamed et al. (Hamed et al. 2020). The precursor solutions for the synthesis of the nanoparticles included silver nitrate hexahydrate ($Na_2S \cdot 6H_2O$) (1.698 g, 0.1 M), sodium sulfide (0.4 g, 0.1 M), and polyvinyl pyrrolidone (PVP) (3.0 g), which were separately dissolved in double-distilled water (50 mL) at room temperature. Sodium sulfide and the PVP solutions were dispensed dropwise into the silver nitrate solution while being stirred with a magnetic stirrer for 3 more hours. The obtained precipitate was put in a centrifuge set at 4500 revolutions per minute and centrifuged for 5 min. The precipitate obtained after centrifugation was washed with ethanol and then with double-distilled water till it had a neutral pH. The residue was then dried in an oven for 3 h at 80 °C to obtain Ag_2S NPs. For the synthesis of the Ag_2S-rGO nanocomposite, GO dispersions of 10, 100, and 150 mg in 10, 100, and 150 ml of double-distilled water, respectively, was injected into silver nitrate, PVP, and sodium sulfide mixture and stirred for one more hour.

For the synthesis of the Ag_2S-rGO nanocomposite, GO at dispersions of 10, 100, and 150 mg in 10, 100, and 150 ml of double-distilled water, respectively, was injected into a silver nitrate, PVP, and sodium sulfide mixture and stirred for one more hour. The various GO dispersions yielded varied rGO loadings in the Ag_2S-rGO nanocomposite. The solution obtained was centrifuged at 4500 revolutions per minute for five minutes and successively washed in ethanol and double-distilled water. The residue was vacuum-dried for 8 h at 80 °C to get the nanocomposite.

Solar cells fabrication

Ag_2S-rGO nanocomposite was employed in the photoactive layer (P3HT: PCBM) and HTL of the OSC. For the HTL, the Ag_2S-rGO nanocomposite at concentrations of 20 wt.% and 30 wt.% was dispersed in PEDOT: PSS by stirring at 40 °C overnight to achieve a homogenous solution. The solutions for the active layer were prepared in 20 mg/mL concentrations of chloroform from P3HT: PCBM at a ratio of 1:1 and Ag_2S-rGO at various concentrations of 10, 20, and 30 wt.%, then stirred at 40 °C for 3 h.

The fabricated Bulk Heterojunction Organic Solar Cells (BHJ-OSC) devices were structured as glass/ITO/PEDOT: PSS-Ag_2S-rGO/P3HT: PCBM/LiF/Al for modified HTL (Figure 1a). Similarly, the architecture of the devices whose photoactive layers were modified was glass/ITO/PEDOT: PSS/P3HT:PCBM: Ag_2S-rGO/LiF/Al (Figure 1b). ITO-coated glass substrates of 15 Ω/sq sheet resistance were cleaned before coating the different layers. The glass substrates were cleaned by ultrasonication in boiled deionized water with soap. The cleaning went on with ultrasonication of the substrates in the order of 10 min in deionized water, acetone, and isopropanol. The substrates were

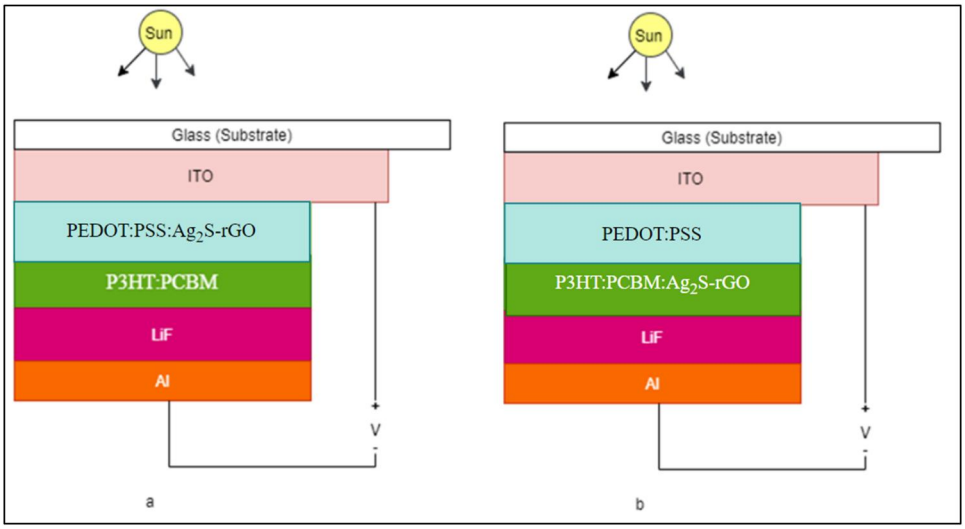

Figure 1. BHJ-OSC Devices with modified (a) HTL and (b) photoactive layer.

transferred to an oven for drying at 120 °C for 30 min. Spin coating of PEDOT: PSS- Ag_2S-rGO HTL was done for 60 s at 4500 rpm. P3HT: PCBM and P3HT:PCBM: Ag_2S-rGO were subsequently spin-coated for 60 s at 1200 rpm on the PEDOT: PSS- Ag_2S-rGO and PEDOT: PSS HTLs, respectively, followed by annealing under a flow of nitrogen gas for 5 min at 120 °C. The deposition of LiF (0.4 nm) and Al (50 nm) on the substrates was performed by thermal evaporation in a vacuum at a pressure of 10^{-6} mbar (Using EDWARDS AUTO 306 TURBO thermal evaporator). Reference devices with PEDOT: PSS HTL and P3HT: PCBM active layer were also fabricated for comparison purposes. The devices were all fabricated with an active layer of 0.04 cm^2 under ambient conditions.

Characterization

The morphological properties of the nanocomposite were determined using the field emission scanning electron microscope (SEM: Phenom Pro by Thermofisher) and Transmission Electron Microscopy (TEM: JEOL JEM 1010). The materials were also analyzed for elemental composition using an EDX detector fitted on SEM (Phenom Pro by Thermofisher). The structural analysis was carried out with XRD (MiniFlex 300/600) by Cu kα source of radiation ($\lambda = 1.5418740$ Å) from 10° to 90° scan, having 10°/min scan speed. Perkin Elmer Spectrum 100 Fourier transform infrared (FTIR) spectrometer (FTIR) was used, and the infrared (IR) spectra of the samples were recorded. A UV-Vis spectrophotometer (UV-1900i by Shimadzu) was employed in determining the optical transmittance and absorbance of the samples. In order to carry out optic absorption measurements, nanomaterials were dispersed in ethanol.

The HTL and photoactive layer materials were deposited on ITO substrates, and transmission and absorption spectra of the materials were obtained using by UV-Vis spectrophotometer. A source meter (Ossila Source Measure X-200) at solar simulator (SCIENCETECH SciSun-150 class AAA) at 100 mW/cm^2 integrated power density and AM 1.5 was used to determine the current density versus voltage (J-V) characteristic of fabricated solar cells.

Results and discussion

Morphological properties

Figure 2, the SEM image of the nanocomposite, shows a tightly packed structure of folded rGO around the nanowire-shaped Ag_2S. The importance of this structure is that rGO becomes uniformly distributed onto the surface of the Ag_2S, hence obtaining homogeneity in the synthesized nanocomposite. When GO gets chemically reduced to rGO, through the chemical reduction method, vacancies and defect sites are produced in the carbon structure (Pan et al. 2011). Homogeneity of the nanocomposite is further achieved by having the crystals of Ag_2S grow around these vacancies and defect sites. Figure 3 shows the morphology of Ag_2S nanoparticles to be in a nanowire shape. The nanowires of Ag_2S possess unique mechanical, optoelectronic, and electrical properties (Sadovnikov and Gusev 2017). Optoelectronic properties of Ag_2S nanowires display high optical transmission and low sheet resistance and are in line with OSC needs (Khanarian et al. 2013).

TEM was used to examine the internal morphology and distribution of Ag_2S nanoparticles on rGO. Figure 4 reveals dark and high contrast Ag_2S nanoparticles uniformly distributed on lighter and transparent matrices of rGO sheets. This observation is consistent with the existing evidence that 2-D morphology of graphene under

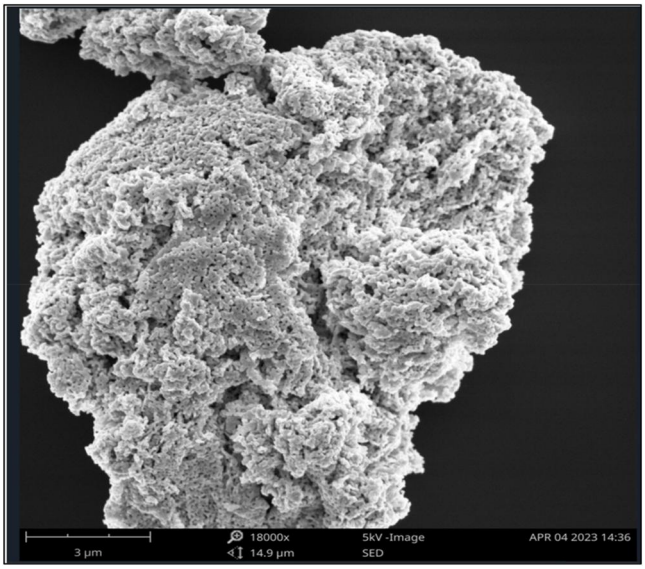

Figure 2. SEM image of Ag_2S-rGO with rGO concentration of 10 mg.

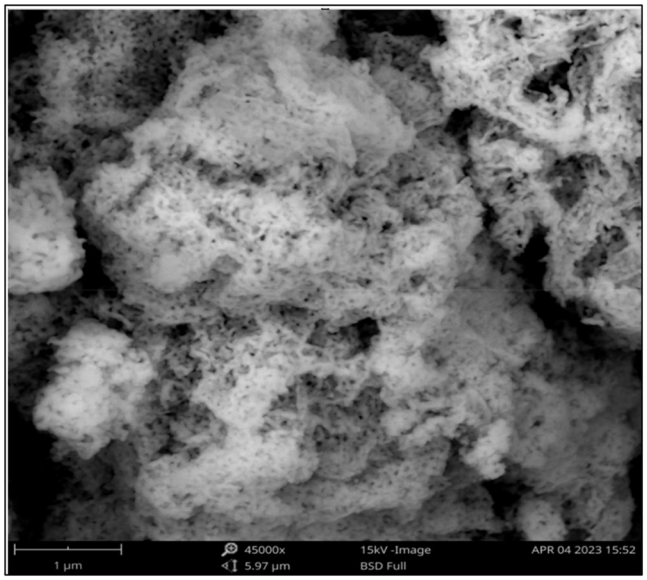

Figure 3. SEM image of Ag_2S-rGO with GO concentration of 150 mg.

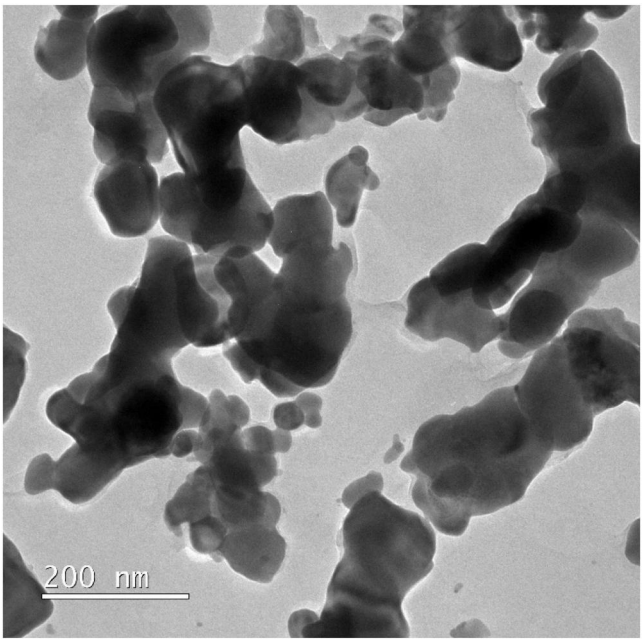

Figure 4. TEM analysis of Ag_2S-rGO nanocomposite.

TEM appears as transparent sheets, while Ag nanoparticles are spherical and attached onto rGO (Tran et al. 2020).

SEM-EDX analysis

The elemental analysis of the Ag_2S-rGO nanocomposite from SEM-EDX is shown in Figure 5 and Table 1. The spectrum confirms the predominance of C, Ag, O, and S in the nanocomposite, indicating the successful formation of the Ag_2S-rGO nanocomposite. The rGO component in the nanocomposite material shows its presence by detecting O and C peaks in the spectrum. The synthesis process successfully reduced GO based on the single weak O peak detected in the analysis. Figure 5 demonstrates that the elements within the rGO matrix are spread evenly throughout its structure rather than being restricted to specific areas (Sadovnikov and Gusev 2017). The nanocomposite demonstrates homogeneous composition because its elements are uniformly distributed.

Structural properties

The XRD spectrum for the Ag_2S NPs and Ag_2S-rGO nanocomposite is shown in Figure 5. The XRD spectrum of Ag_2S NPs showed peaks at 2θ values of 17.2°, 22.4°, 24.9°, 25.9°, 26.3, 28.9°, 31.5°, 33.6°, 34.38°, 34.7°, 36.8°, 37.7°, 40.7°, 43.4°, 46.2°, 47.8°, 48.7°, 53.2°, and 58°. These diffraction peaks correspond to (011), (10-1), (110), (11-1), (022), (021), (111),(120), (120), (−121), (112), (013), (−113), (122), (210), (20-2), (113), (220), (221), and (−142) lattice planes of Ag_2S according to JCPDS card 96-900-0254 (Wiegers 1971). The diffraction peaks from XRD analysis show that Ag_2S NPs exist as a monoclinic acanthite phase. XRD results show that the synthesized Ag_2S exists as nanoparticles with diffraction line d-spacings between 1.0 and 5.2 Å. Match! Software™ enabled the determination of the d-spacing. The XRD data analysis utilized Match! Software™ for the analysis.

The nanocomposite XRD pattern in Figure 6(b) shows additional peaks at 2θ values of 26.3°, 44.3°, 54.2°, 83.2°, and 85.0° to the ones for Ag_2S NPs in Figure 6(a) that match with the (002), (101), (400), (112), and (006) crystalline planes of GO according to JCPDS-card 01-075-1621. The $2\theta = 26.3°$ peak in the XRD pattern represents (002) carbon peaks with 3.395 Å d-spacing that matches Ag_2S NPs (022) planes to show uniform nanocomposite formation (de Moraes et al. 2015). XRD analysis shows that the GO characteristic peaks below 12.0° disappeared after the successful chemical reduction of GO during the chemical reduction process (Baskar et al. 2016; Vi et al. 2018).

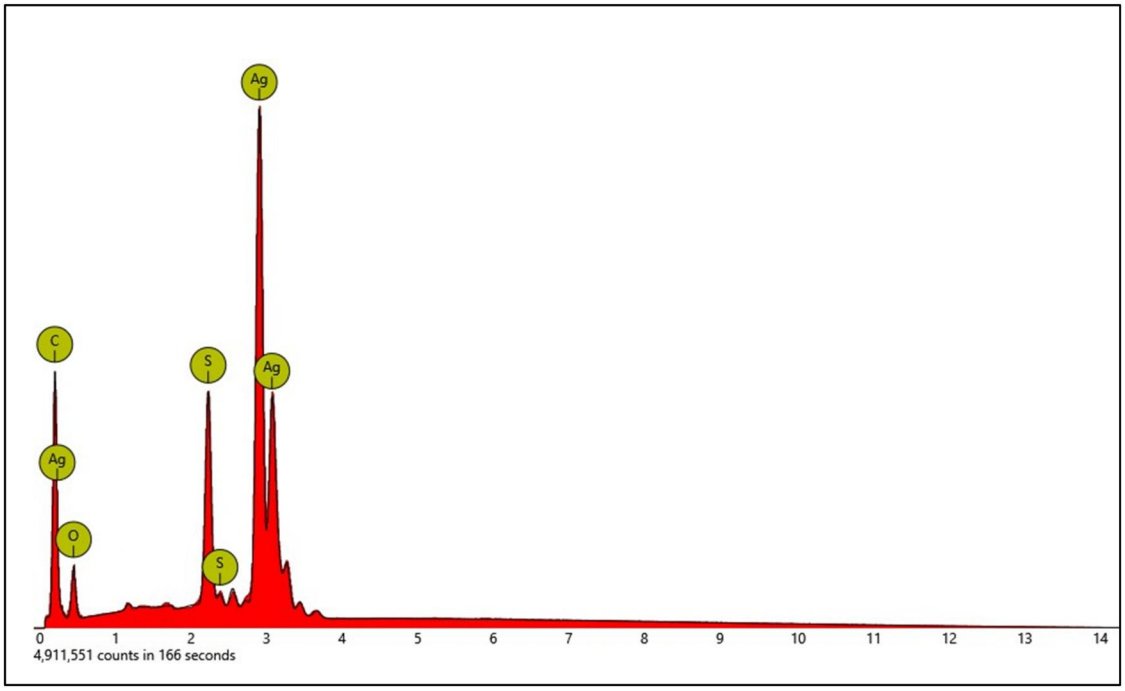

Figure 5. SEM-EDX analysis of Ag_2S-rGO nanocomposite.

Table 1. EDX elemental composition (wt %) of Ag_2S-rGO nanocomposite.

Element	Atomic concentration (%)	Weight concentration (%)
Carbon	52.20	17.53
Silver	22.46	67.73
Oxygen	17.59	7.87
Sulfur	7.43	6.66
Magnesium	0.32	0.22

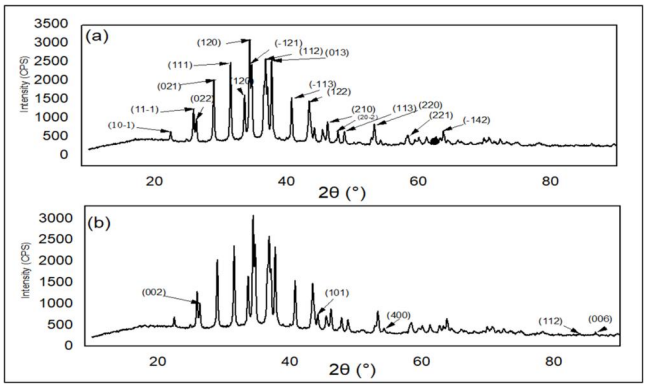

Figure 6. XRD patterns for (a) Ag_2S NPs and (b) Ag_2S-rGO nanocomposite.

Optical absorption

The Ag_2S NPs and Ag_2S nanocomposite UV-Vis spectra are shown in Figure 7. A common absorption peak appears at 202 nm for the Ag_2S nanoparticles and Ag_2S-rGO nanocomposite. For Ag_2S NPs, this peak resonates with the plasmon resonance of the nanowire-shaped nanoparticles (Delgado et al. 2018). Nanowire-shaped Ag_2S-rGO, shown in Figure 3, uses LSPR to trap light effectively (Smith et al. 2019). Figure 7(b) shows a peak at 202 nm, indicating superimposition of the absorbance of Ag_2S and rGO. The absorbance peak at 202 nm also demonstrates π-π^* transitions of the C-C aromatic bonds for rGO (Cui et al. 2015; Kumar et al. 2019; Amollo et al. 2020).

Photoactive layer modification

The active layer optical absorption

Since one problem with OSCs is low photon absorption, the active layer of the device was examined for its optical absorption. The acceptor material of the photoactive layer, PCBM, is known to have low light absorption, causing low efficiency of the OSCs (Manzano et al. 2015). High light absorption in the photoactive layer is necessary for enhanced photogeneration of the charger carriers (Amollo et al., 2018). Figure 8 shows the UV-Vis absorbance spectra for the photoactive layers of P3HT: PCBM with Ag_2S-rGO nanocomposite added at (a) 10 wt% and (b) 30 wt% concentrations. From this section, the nanocomposite prepared with GO of 100 mg and 150 mg dispersed in 100 and 150 ml of distilled water and injected into

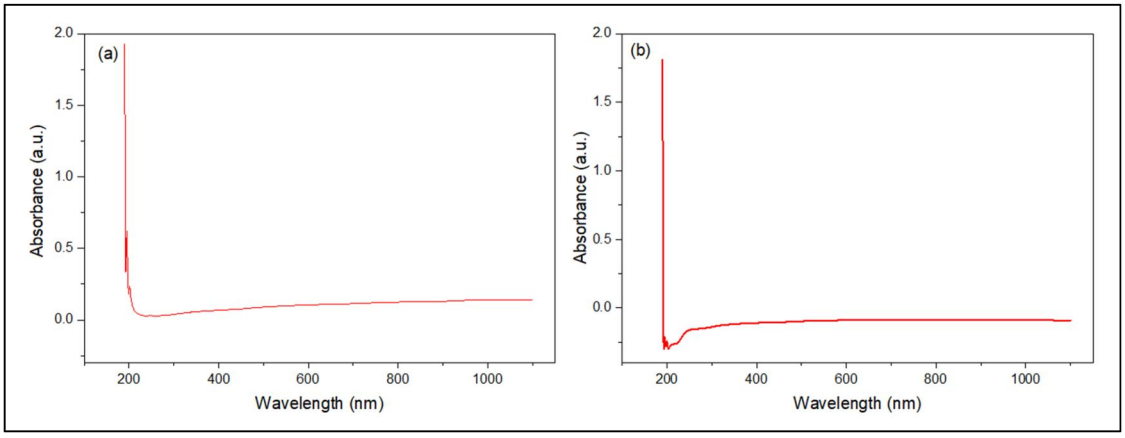

Figure 7. Optical absorption of (a) Ag_2S NPs and (b) Ag_2S-rGO nanocomposite.

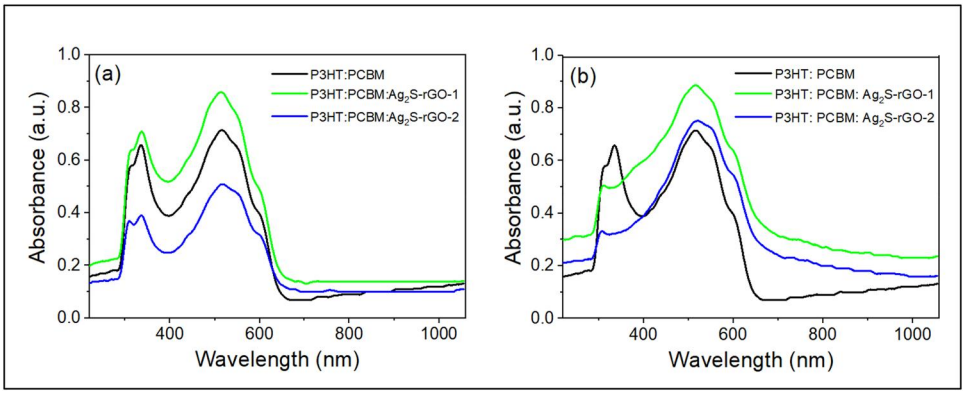

Figure 8. UV-vis absorbance spectra for P3HT: PCBM photoactive layers with (a) 10 wt% and (b) 30 wt% loadings of Ag_2S-rGO.

the Ag_2S precursor mixture will be referred to as Ag_2S-rGO-1 and Ag_2S-rGO-2, respectively.

At 10 wt.%, the photoactive layer with Ag_2S-rGO-1 demonstrated the strongest absorption compared to the pure P3HT: PCBM and Ag_2S-rGO-2 in the visible region. Active layers with Ag_2S-rGO-1 and Ag_2S-rGO-2 show higher absorption within the visible region than the non-modified devices at 30 wt.% loadings (Figure 8b).

The observable stronger absorption peaks of the active layers with Ag_2S-rGO-1 at 10 and 30 wt.% and Ag_2S-rGO-2 at 30 wt.% compared to P3HT: PCBM can be attributed to the contribution of rGO and Ag_2S NPs in the nanocomposite. At optimal concentration, rGO minimizes the torsional disorders of the P3HT chains, thereby causing an increase in its conjugational length (Bkakri et al. 2015). This implies increased alterations of the single-double bonds within the chains of the polymer (Ismail et al. 2015), which leads to improved photon absorption, thereby increasing the charge carrier generation in the OSCs. The nanocomposite also enhances the absorption peaks of the P3HT: PCBM in the UV regions due to the presence of Ag_2S NPs in the nanocomposite (Hamed et al. 2020). It is observable from Figure 8 that films with Ag_2S-rGO-1 at 10 wt.% have higher absorption peaks at 338 and 515 nm, and Ag_2S-rGO-2 at 30 wt.% have high absorbance peaks at 515 nm. The peaks within the UV region are contributed to by the surface plasmon polarization resonance characteristic of the Ag_2S surface's collective conductive electron oscillation (Hamed et al. 2020). However, the peaks in the visible regions can be related to the contribution from the surface distribution of Ag_2S sizes that increases the surface scattering and states (Hamed et al. 2020). The absorption peak is more intense in the visible than in the UV region, showing that Ag_2S gets more activated in the visible than in the UV region,

thereby enhancing light absorption (Cui et al. 2015). The lower absorption of the active layers with Ag_2S-rGO-2 at 10 wt.% than the reference device can be explained by the possibilities of agglomeration of the graphene layers in the nanocomposite, since Ag_2S-rGO-2 has a higher rGO concentration than Ag_2S-rGO-1 at 10 wt.%. The agglomeration of graphene sheets in the device reduces the P3HT lamellae's degree of order, reducing the devices' absorption properties (Bkakri et al. 2015). Hence, the absorption of light improves with addition of the nanocomposite to OSCs' photoactive layer depending on the concentration of rGO in the nanocomposite and the overall weight loading of the nanocomposite to the polymer matrix.

The spectrum of light the OSCs absorb becomes a little wider when the nanocomposite is put in the active layer. Figure 8(b) shows that at 30 wt.% loading, all the modified devices with all the concentrations of rGO in the nanocomposite showed a lower absorption onset at about 332 nm compared to the reference device, which starts at 395 nm, corroborant with the findings of (Amollo et al., 2018). The broadening of the absorption spectrum is attributed to the Ag_2S-rGO nanocomposite contribution to the active material's polymer matrix. The slightly broadened absorption spectrum implies that the donor polymer has a lowered bandgap (Amollo et al. 2020). A lowered bandgap means an increase in photogeneration of charge carriers, hence better performance of the solar cells. Nanocomposites with Ag_2S NPs as one of their components have shown improved spectrum utilization (Kumar et al. 2019).

Optical transmittance of the HTL

Figure 9 shows the optical transmittance spectra of PEDOT: PSS: Ag_2S-rGO coated on an ITO substrate. At 20 wt.% loading of the nanocomposite, the reference, and the PEDOT: PSS: Ag_2S-rGO-1 showed the same highest transmittance of 100% at 327 nm (Figure 9a). It is expected that the incorporation of the Ag_2S-rGO-1 and Ag_2S-rGO-2 at 20 and 30 wt.% to the PEDOT: PSS HTL will not adversely affect the light transmittance and absorption in the HTL and the photoactive layer, respectively, within the UV region but slightly lowers the transmittance in the visible region. At 20 wt.%, PEDOT: PSS: Ag_2S-rGO-2 had a lower transmittance of light of 94% at about 327 nm wavelength compared to the reference and PEDOT: PSS: Ag_2S-rGO-1 HTLs. At 30 wt.% (Figure 9b), all the modified HTLs had a lower transmittance compared to the reference HTL in both the UV and the visible regions. The increased photon absorption by the nanocomposite can explain the lower transmittance of the modified HTL. Silver nanoparticles are known to trap light through LSPR, which could have contributed to the absorption of some light in the modified HTL (Hamed et al. 2020). The rGO in the nanocomposite also has high optical absorbance, lowering the transmittance of the modified HTL (Amollo et al., 2018). The strong absorbance of rGO also explains why, within the visible region, the modified HTL exhibited lower transmittance with the increase in the concentration of rGO in the nanocomposite for both the 20 and 30 wt.% loadings of the nanocomposite.

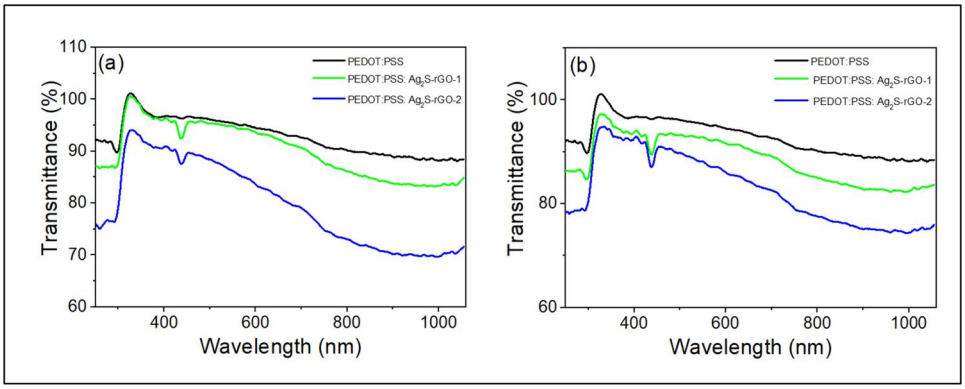

Figure 9. UV-vis transmittance spectra of PEDOT: PSS HTL with (a) 20 wt% and (b) 30 wt% loadings of Ag_2S-rGO.

The modified HTLs have a dip in transmittance at about 435 nm for both 20 wt.% and 30 wt.% loadings, which the reference HTL does not have. The silver nanoparticles' dipole plasmon resonance explains this drop in transmittance since silver nanoparticles absorb light at about 435 nm (Ahmad et al. 2020). In BHJ, the active layer and HTL both contend for light absorption, explaining why the optical properties of the latter influence those of the former (Hou et al. 2015). Nonetheless, the generation of excitons in the BHJ devices only results from the light absorbed in the photoactive layer. The incorporation of Ag_2S-rGO nanocomposite into the HTL changes the surface energy and wettability (Nguyen et al. 2022), which allows for a more ordered and uniform morphology of the photoactive layer, thereby improving the optical absorption and charge generation and transport.

Solar cells characterization

Hole transport layer

All the devices with the nanocomposite in the HTL demonstrated a significant improvement in their photovoltaic performances, as seen in Table 2. The device *J-V* characteristics for the modified HTL are shown in Figure 10. As shown in Table 2, the PCE, FF, and J_{sc} were significantly improved with the increase in the concentration of rGO in the nanocomposite at 20 wt% loading of the nanocomposite to the HTL material. The introduction of the Ag_2S-rGO to the HTL caused a higher current density, which enhanced the device's performance (Amollo et al., 2018). Another research showed that the J_{sc} increased from 10 to 11.0 mA cm^{-2} after introducing silver nanoparticles into PEDOT: PSS in OSCs, thereby improving the PCE to 2.0% from 1.7% (Rivera-Taco et al. 2021). The nanocomposite also increased the photoactive and HTL interfacial area (Rivera-Taco et al. 2021). The increased interfacial area implies an improved efficiency of how the anode collects holes, further improving the J_{SC} of the OSC devices. Doping PEDOT: PSS with silver nanoparticles increased its electrical conductivity from 0.5 to 200 Scm^{-1} (Rivera-Taco et al. 2021). The observed performance enhancement of the devices with modified HTL, therefore, demonstrates that the Ag_2S-rGO nanocomposite improved the charge extraction at the photoactive layer and the HTL interface. The

Table 2. Photovoltaic parameters of modified HTL with different loadings of Ag_2S-rGO.

Nanocomposite concentration (wt.%)	HTL material	PCE (%)	FF (%)	J_{sc} (mA cm^{-2})	V_{oc} (volts)	R_s (Ω)
Reference	PEDOT: PSS	1.5	41	6.9	0.55	152
20	PEDOT: PSS: Ag_2S-rGO-1	1.9	31	11	0.55	34
	PEDOT: PSS: Ag_2S-rGO-2	2.0	32	12	0.54	30
30	PEDOT: PSS: Ag_2S-rGO-1	2.3	35	12	0.53	20
	PEDOT: PSS: Ag_2S-rGO-2	1.7	33	10	0.50	25
	PEDOT: PSS: GO	1.8	26	8	0.50	47
	PEDOT: PSS: Ag_2S	2.1	26	11	0.55	35

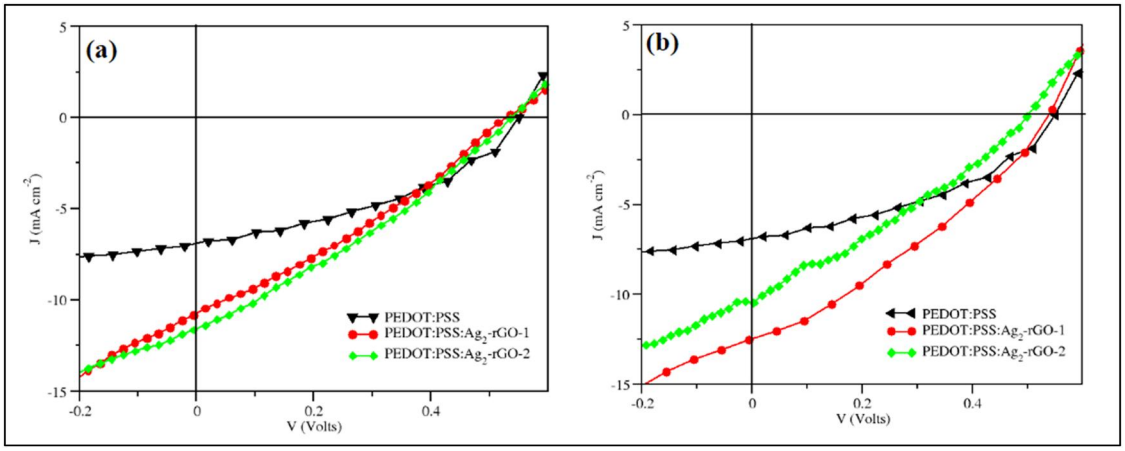

Figure 10. The J-V characteristics of the PEDOT: PSS HTL with (a) 20 wt.% and (b) 30 wt.% loadings of Ag_2S-rGO.

nanowire shape of Ag_2S offers plasmon-induced charge separation while the rGO sheets within the nanocomposite creates charge transfer pathways (Amollo 2024) for electron transport and large surface area at the interfaces. These properties facilitate charge dissociation, yield enhanced charge transport, reduced charge recombination, and thus resulting in better extraction of charges.

It is instructive to consider the energy level alignment of the devices with the Ag_2S-rGO nanocomposite modification. As shown in Figure 11. The incorporation of Ag_2S-rGO introduces a shifted HOMO at approximately −4.9 eV, while for non-modified devices, the energy level of the HOMO of P3HT is −5.0 and −5.2 eV for PEDOT:PSS (Ryu et al. 2023). Thus, the nanocomposite creates a favorable stepped alignment, which reduces the barrier to hole extraction at the interface. The rGO component acts as a conductive bridge, which facilitates a faster charge transport as Ag_2S nanowires provide high surface area pathways for the movement of charge carriers. Figure 11 shows how the introduction of the nanocomposite to the HTL enhances electron extraction and reduces charge carrier recombination within the photovoltaic blend. The energy level dynamics corroborate with the observed J_{sc} increase and the 53% increase in efficiency of the HTL-modified devices compared to the non-modified devices.

In addition to better energy-level alignment, rGO has high electrical conductivity, assisting in preventing trap-assisted recombination. rGO has a sp^2 carbon structure, which offers charge transport pathways. Combined with the nanowire shape of Ag_2S, the nanocomposite results in a reduced carrier residence time within the

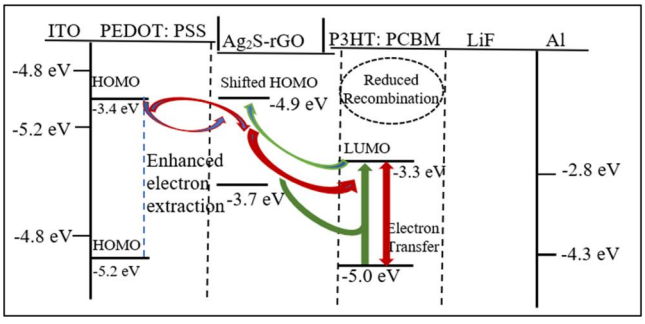

Figure 11. Energy level diagram of how Ag_2S–rGO modifies the HTL band structure.

interfacial trap positions and reduced charge trap densities. The increased FF and reduced series resistance of the nanocomposite in the modified HTLs evidence this effect, demonstrating that rGO conductivity is a significant factor in achieving a downward trend of trap-assisted recombination and an upward trend of efficient charge extraction.

At rGO loading of 30 wt.%, the PCE and J_{sc} of the devices with modified HTL went down as the rGO concentration went up in the nanocomposite. Although the PCE for the devices with Ag_2S-rGO-1 and Ag_2S-rGO-2 nanocomposites, at 30 wt.% loading, in the HTL is higher than for the pristine PEDOT: PSS HTL devices, Ag_2S-rGO-2 demonstrated less PCE, FF, V_{oc}, and J_{sc} compared to the devices with Ag_2S-rGO-1 (Table 2). The best-performing device with modified HTL was demonstrated to be the one with Ag_2S-rGO-1 nanocomposite at 30 wt.% loading, while the lowest-performing device has Ag_2S-rGO-2 at 30 wt.% loading in the HTL. The low performance of the devices with Ag_2S-rGO-2 in the HTL can be attributed to higher recombination of the charge carriers in the device (Amollo et al., 2018). The higher loss in charger carriers is also observed from the higher R_S for devices with Ag_2S-rGO-2 in HTL compared to those with Ag_2S-rGO-1.

As the concentration of rGO increases in the nanocomposite and thus the device, agglomeration of the nanocomposite occurs, which impedes the charge carrier transport to the anode (Amollo et al. 2020). Ag_2S-rGO-2 at the HTL gives the device better performance than the reference device because rGO forms a low barrier for charge injection (Li et al. 2010). Because of the low injection barrier, it is simple to have an injection of holes at the HTL and collect them at the anode.

To isolate the synergic effects, the device performance was compared with GO-only and Ag_2S-only HTL modifications at 30 wt.% loadings (Table 2). The GO-only device demonstrated significant improvement in efficiency compared to the reference device due to improved interfacial contact. However, the GO-only HTL devices demonstrated considerably lower FF (from 41% to 26%), an indicator of limited charge transport.

Devices with only Ag_2S on the HTLs, however, demonstrated an enhanced $J_{sc,}$ a demonstration of improved charge extraction and low FF, demonstrating an increased interfacial charge recombination (Table 2). Devices with Ag_2S-rGO modified HTLs had the highest PCE and lower series resistance and improved FF, showing simultaneous improvement of charge transport and interfacial contact. The Comparison demonstrates that the synergic interaction between GO and Ag_2S results in superior device performance compared to either component alone.

Photoactive layer

Table 3 provides the photovoltaic parameters for devices made with 10, 20, and 30 wt.% nanocomposites in the photoactive layer. The *J-V* curves of the devices are presented in Figure 12. All the devices with the modified photoactive layers had better performance than the reference devices. All the devices with Ag_2S-rGO added to the photoactive layer exhibited enhanced J_{sc} and PCE. The enhanced J_{sc} is associated with improved charge generation, collection, and transport due to incorporating the nanocomposite into the photoactive layer (Amollo et al. 2020). The improved J_{sc} resulted in a substantial improvement of the PCE after the nanocomposite was added to the photoactive layer.

The improved solar cell device performance, as observed in Figure 12, can be explained by the strong absorbance of the modified solar cell devices with Ag_2S-rGO-1 at 10 wt.% and Ag_2S-rGO-1 and Ag_2S-rGO-2 at 30 wt.%. In addition to the effective generating of excitons, their optimal dissociation and transportation to the electrodes determine the performance of OSCs (Amollo et al., 2018). Although devices with Ag_2S-rGO-2 at 10 wt.% had lower absorbance than the reference device within the visible region (Figure 8a), they still had higher performance than the reference solar cell, implying improved charge separation and transport.

Even though adding the Ag_2S-rGO-2 nanocomposite to the photoactive layer improves the devices' PCE, FF, and J_{sc}, as indicated in Table 3, the efficiency decreases with an increase in the wt.% loading. The PCE (and FF) of the solar cells with Ag_2S-rGO-2 in the photoactive layer decreases from 2.6% (34) to 2.5% (32) and 2.1% (31) for 10, 20, and 30 wt.% loadings, respectively. This declining performance can be associated with the possibility of the Ag_2S-rGO nanocomposite forming agglomerates on the active layer film; the agglomerates act as charge traps to cause charge carrier loss. On the contrary, the PCE of the devices with Ag_2S-rGO-1 increased with the increase in wt.% loading in the photoactive layer. The PCE increased from 2.5% for 10 wt. % loading to 2.8% for 20 wt.% loading and to 3.4% for 30 wt.% loadings, respectively.

According to Table 3, the FF of devices with 20 wt.% Ag_2S-rGO-1 in the photoactive layer is less than that of devices made with pristine P3HT: PCBM as the photoactive layer material. Lowering of FF means there is a chance of current leakages through short-circuit routes (Amollo et al. 2020). These current leakages occur in local defect states. A possible source of losses in charge carriers is the imbalance in the mobility of the carriers in the BHJ blend of the photoactive layer (Smith et al. 2014). So, the better PCE of devices with modified photoactive layers, as shown in Figure 8(b), is due to the stronger optical absorption (where devices with Ag_2S-rGO-1 demonstrate the highest optical absorbance compared to Ag_2S-rGO-2 and reference devices) and a subsequent photogeneration of charge carriers, indicated by improved J_{sc}.

Table 3. Photovoltaic parameters of the modified photoactive layers at different loadings of Ag_2S-rGO.

Nanocomposite concentration (wt.%)	Active layer material	PCE (%)	FF (%)	J_{sc} (mA cm^{-2})	V_{oc} (volts)	R (Ω)
Reference	P3HT: PCBM	1.5	41	6.9	0.55	152
10	P3HT: PCBM: Ag_2S-rGO-1	2.5	30	9.9	0.51	46
	P3HT: PCBM: Ag_2S-rGO-2	2.6	34	15	0.52	24
20	P3HT: PCBM: Ag_2S-rGO-1	2.8	27	11	0.55	41
	P3HT: PCBM: Ag_2S-rGO-2	2.5	32	14	0.54	18
30	P3HT: PCBM: Ag_2S-rGO-1	3.4	33	17	0.59	22
	P3HT: PCBM: Ag_2S-rGO-2	2.1	31	12	0.57	29

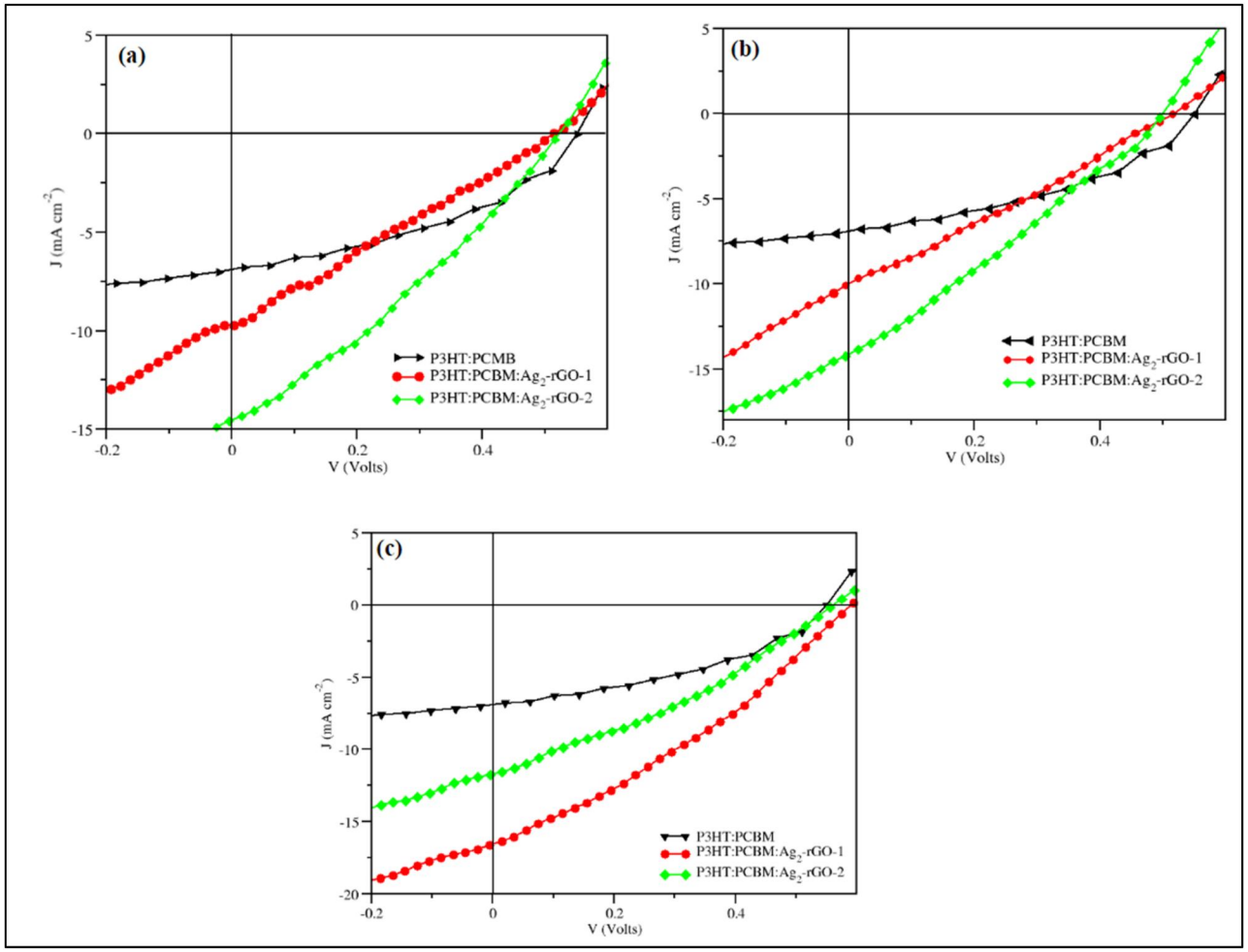

Figure 12. The J-V characteristics of the P3HT: PCBM photoactive layer with (a) 10 wt.%, (b) 20 wt.%, and (c) 30 wt.% loadings of Ag_2S-rGO.

Table 4. Stability of reference device.

Elapsed time (hrs)	PCE (%)	FF (%)	J_{sc} (mA cm^{-2})	V_{oc} (volts)	R (Ω)
0	1.5	41	6.9	0.55	152
6	1.48	31	5.7	0.54	79
12	1.42	30	5.7	0.54	63
18	1.32	31	5.7	0.52	76
24	1.19	30	5.7	0.53	76

Table 5. Stability of PEDOT: PSS: Ag_2S-rGO-1 at 30% wt.% loading in HTL.

Elapsed time (hrs)	PCE (%)	FF (%)	J_{sc} (mA cm^{-2})	V_{oc} (volts)	R (Ω)
0	2.3	35	12	0.53	20
6	2.3	31	11.7	0.58	43
12	2.3	31	10.5	0.53	32
18	2.2	29	10.8	0.53	35
24	2.0	29	10.2	0.51	37

Table 6. Stability of P3HT: PCBM: Ag_2S-rGO-1 at 30% wt.% loading in photoactive layer.

Elapsed time (hrs)	PCE (%)	FF (%)	J_{sc} (mA cm^{-2})	V_{oc} (volts)	R (Ω)
0	3.4	33	17	0.59	22
6	3.3	28	14	0.58	40
12	3.1	30	14	0.58	32
18	3.1	29	14	0.57	38
24	3.0	27	14	0.56	36

Stability measurements

Tables 4–6 and show the operational stability of the OSC devices obtained by tracking their photovoltaic parameters over 24 h. The reference device containing pristine PEDOT: PSS shows degradation, with the PCE reducing from 1.5% to 1.19% over 24 h, retaining 79% of its efficiency. The j_{sc} and the series resistance also change considerably, indicating interfacial and morphological instability. Devices with the nanocomposite demonstrated better stability. The Ag_2S-rGO-1 modified HTL retained 87% of its PCE after 24 h with a relatively constant v_{oc} and FF showing suppressed charge accumulation and reduced interfacial charge recombination. Likewise, devices

Table 7. Photovoltaic parameters of OSCs with modified active and hole transport layers.

Previous work	Device architecture	PCE (%)	FF (%)	J_{sc} (mA cm^{-2})	V_{oc} (volts)
This work	ITO/PEDOT:PSS/P3HT:PCBM:Ag_2S-rGO-1 (at 30% wt.%)/LiF/Al	3.4	33	17	0.59
This work	ITO/PEDOT:PSS:Ag_2S-rGO-1(at 30% wt.%)/P3HT:PCBM/ LiF/Al	2.3	35	12	0.53
Amollo et al. (2018)	ITO/PEDOT:PSS/P3HT:PCBM:GO/LiF/Al	4.4	43	18.2	0.57
Hamed et al. (2020)	ITO/ZnO/P3HT:PCBM:Ag_2S/MoO_3/Al	5.13	56.25	15.91	0.57
Rivera et al. (2021)	ITO/PEDOT:PSS:Ag-NPs/PBDB-T:ITIC/PFN/FM	6.4	49	15.5	0.84
Gavim et al. (2025)	ITO/PEDOT:PSS/AgNPs/PM6:Y6/PDINN/Ag	13.0	68.6	23.1	0.82

with Ag_2S-rGO-1 modified photoactive layers demonstrated 88% PCE retention after 24 h. Enhanced stability of the devices with the nanocomposite can be attributed to the fact that graphene-based interlayers have reduce moisture degradation in OSCs (Hou et al. 2015). Adding conductive nanostructures, such as Ag nanoparticles, stabilizes the activities of OSCs by minimizing trap-assisted recombination (Rivera-Taco et al. 2021). The migration of Ag can be an issue in organic devices. However, the presence of Ag in the chemically stable phase of Ag_2S and its incorporation on the rGO sheets effectively inhibits its diffusion into the photoactive layer, as demonstrated by increased stability of the devices with Ag_2S-rGO modification.

Comparison with previous work

Table 7 compares the photovoltaic performance of the solar cell devices in this study and previous works on OSCs with Ag, Ag_2S, or GO-based modifications. The recorded performance of the previous works is based on the best-performing devices. The PCE for the Ag_2S-rGO modified HTL and active layer increased by 53% and 127%, respectively, which is relatively above what previous studies have found. For instance, Amollo et al. (2018) and Hamed et al. (2020) reported a 120% increase in PCE after modifying the photoactive layer of OSCs, which is slightly below the 127% of the current work. Rivera-Taco et al. (2021) and Gavim et al. (2025) reported significantly higher efficiencies of 6.4% and 13.0%, an increase of 8.47% and 8.33%, respectively, using non-fullerene acceptors. The meager improvements in efficiencies of such devices reflect the already optimized nature of the systems as opposed to fullerene-based active layers. In this study, the enhancement in performance is primarily based on the pronounced increase in the J_{sc} reaching 17 mAcm^{-2} for the devices with modified active layers, as the V_{oc} remains almost unchanged. This implies that Ag_2S-rGO significantly improves light harvesting and charge transport rather than altering the interfacial energy alignment. This work, therefore, demonstrates that Ag_2S-rGO nanocomposite offers a a substantial improvement of the efficiency of P3HT:PCBM-based OSCs.

Conclusion

The study demonstrated that incorporating Ag_2S-rGO nanocomposites into the photoactive and hole transport layers of P3HT: PCBM-based OSCs significantly enhanced their performance. The nanocomposite was synthesized through a chemical reduction method and demonstrated high crystallinity. The nanowire-shape of the Ag_2S constituent enhances light absorption, while the intercalated rGO sheets contribute to enhanced charge transport. UV-Vis analysis confirmed strong light absorption in the UV and visible regions, with the modified HTLs maintaining adequate optical transmittance. The active layer modified devices demonstrated a PCE increase of up to 127% and the HTL-modified devices showed up to 53% performance improvement. Thus, applying Ag_2S-rGO nanocomposite to the HTL and photoactive layer of the OSCs considerably improves the solar cell's performance by enhancing light harvesting, charge generation, and extraction. The nanocomposite also improved the operational stability of the OSCs.

Acknowledgments

The authors acknowledge the funders of the research work, including the Carnegie Corporation of New York and The World Academy of Sciences (TWAS) (grant no. 20–187 RG/PHYS/AF/AC_I – FR3240314148). The statements made and views expressed are solely the author's responsibility. The authors acknowledge the University of KwaZulu-Natal,

Nanotechnology platform, South Africa, where X-ray Diffraction analysis was done. The authors also acknowledge BESSY II at Helmholtz-Zentrum Berlin (HZB), Germany, for assisting with scanning electron microscopy measurements.

Authors' contributions

Oyugi N. Robert: Conceptualization, Methodology, Investigation, Data analysis, Writing original draft; Tabitha A. Amollo: Conceptualization, Methodology, Project supervision, Funds acquisition, Review and editing the article; Kallen M. Nalyanya: Project supervision, Review and editing the article; Vincent O. Nyamori: Investigation, Review and editing the article; Ndiritu J. Maina: Investigation.

Disclosure statement

The authors declare that there are no conflicts of interest.

Funding

This research was funded by the Carnegie Corporation of New York and The World Academy of Sciences (TWAS) (grant no. 20–187 RG/PHYS/AF/AC_I – FR3240314148). The statements made and views expressed are solely the author's responsibility.

Data availability statement

All the data used in this manuscript are provided herein.

References

Ahmad H, Albaqawi HS, Yusoff N, Reduan SA, Yi CW. 2020. Reduced graphene oxide-silver nanoparticles for optical pulse generation in ytterbium- and erbium-doped fiber lasers. Sci Rep. 10(1):9408. https://doi.org/10.1038/s41598-020-66253-w

Amollo TA, Mola GT, Nyamori VO. 2018. High-performance organic solar cells utilizing graphene oxide in the active and hole transport layers. Sol Energy. 171(5):83–91. https://doi.org/10.1016/j.solener.2018.06.068

Amollo TA, Mola GT, Nyamori VO. 2018. Polymer solar cells with reduced graphene oxide–germanium quantum dots nanocomposite in the hole transport layer. J Mater Sci Mater Electron. 29(9):7820–7831. https://doi.org/10.1007/s10854-018-8781-1

Amollo TA, Mola GT, Nyamori VO. 2020. Improved short-circuit current density in bulk heterojunction solar cells with reduced graphene oxide-germanium dioxide nanocomposite in the photoactive layer. Mater Chem Phys. 254:123448. https://doi.org/10.1016/j.matchemphys.2020.123448

Amollo TA. 2024. Metallic nanoparticles and hybrids of metallic nanoparticles/graphene nanomaterials for enhanced photon harvesting and charge transport in polymer and dye sensitized solar cells. Heliyon. 10(5):e26401. https://doi.org/10.1016/j.heliyon.2024.e26401

Baskar S, Lavanya T, Subramani K, Satheesh K. 2016. Synthesis and characterization of reduced graphene oxide/Ag2S nanocomposites by co-precipitation method using thiourea as sulfur source and reducing agent. Int J ChemTech Res. 9(5):395–401.

Bkakri R et al. 2015. Effects of the graphene content on the conversion efficiency of P3HT: graphene based organic solar cells. J Phys Chem Solid. 85:206–211. https://doi.org/10.1016/j.jpcs.2015.05.020

Cui C et al. 2015. Synthesis and functions of Ag2S nanostructures. Nanoscale Res Lett. 10(1):431. https://doi.org/10.1186/s11671-015-1125-7

de Moraes ACM, Lima BA, Fonseca de Faria A, Brocchi M, Alves OL. 2015. Graphene oxide-silver nanocomposite as a promising biocidal agent against methicillin-resistant Staphylococcus aureus. Int J Nanomed. 10:6847–6861. https://doi.org/10.2147/IJN.S90660

Delgado Y, Martinez CE, Cortez M, Flores NS, Flores M. 2018. Optical properties of silver, silver sulfide and silver selenide nanoparticles and antibacterial applications. Mater Res Bull. 99:385–392. https://doi.org/10.1016/j.materresbull.2017.11.015

Dhuriya D, Kumar B, Chauhan RK. 2016. Recent advancement in organic solar cells and comparison between various structures. In: 2016 International Conference on Emerging Trends in Communication Technologies (ETCT); p. 1–5. https://doi.org/10.1109/ETCT.2016.7882960

Gavim AEX et al. 2025. Ag nanoparticle layer on PEDOT:PSS with optimized energy levels for improving PM6: Y6-based organic photovoltaics. ACS Omega. 10(33):37664–37673. https://doi.org/10.1021/acsomega.5c04247

Hamed MSG, Adedeji MA, Zhang Y, Mola GT. 2020. Silver sulphide nano-particles enhanced photo-current in polymer solar cells. Appl Phys A. 126(3):1–207. https://doi.org/10.1007/s00339-020-3389-8

He Z et al. 2012. Enhanced power-conversion efficiency in polymer solar cells using an inverted device structure. Nature Photon. 6(9):591–595. https://doi.org/10.1038/nphoton.2012.190

Hou X et al. 2015. Improvement of the power conversion efficiency and long term stability of polymer solar cells by incorporation of amphiphilic Nafion doped PEDOT-PSS as a hole extraction layer. J Mater Chem A. 3(36):18727–18734. https://doi.org/10.1039/C5TA03967C

Hummers WS, Offeman R. 1958. Preparation of graphitic oxide. J Am Chem Soc. 80(6):1339–1339. https://doi.org/10.1021/ja01539a017

Ibrahim K, Saeed K, Khan I. 2019. Nanoparticles: properties, applications and toxicities. Arab J Chem. 12(7):908–931. https://doi.org/10.1016/j.arabjc.2017.05.011

Ismail YAM, Soga T, Jimbo T. 2015. Effect of composition on conjugation structure and energy gap of P3HT: PCBM organic solar cell. Int J New Horizons Phys. 2(2):87–93. https://doi.org/10.12785/ijnhp/020208

Kareem MA et al. 2020. Green synthesis of silver nanoparticles (AgNPs) for optical and photocatalytic applications: a review. IOP Conf Ser Mater Sci Eng. 805(1):012020. https://doi.org/10.1088/1757-899X/805/1/012020

Khalil A, Ahmed Z, Touati F, Masmoudi M. 2016. Review on organic solar cells. In 2016 13th International Multi-Conference on Systems, Signals & Devices (SSD), pp. 342–353. https://doi.org/10.1109/SSD.2016.7473760

Khanarian G et al. 2013. The optical and electrical properties of silver nanowire mesh films. J Appl Phys. 114(2):1–15. https://doi.org/10.1063/1.4812390

Kumar S, Kumar J, Narayan Sharma S, Srivastava S. 2019. rGO Integrated MEHPPV and P3HT polymer blends for bulk hetero junction solar cells: a comparative insight. Optik (Stuttg). 178:411–421. https://doi.org/10.1016/j.ijleo.2018.09.148

Kumari P, Chandran P, Khan SS. 2014. Synthesis and characterization of silver sulfide nanoparticles for photocatalytic and antimicrobial applications. J Photochem Photobiol B. 141:235–240. https://doi.org/10.1016/j.jphotobiol.2014.09.010

Li S-S, Tu K-H, Lin C-C, Chen C-W, Chhowalla M. 2010. Solution-processable graphene oxide as an efficient hole transport layer in polymer solar cells. ACS Nano. 4(6):3169–3174. https://doi.org/10.1021/nn100551j

Liu X-S, Bo Z-M, Tu W-C, Lin M-Y, Chen S-L. 2017. Enhanced performance of reduced graphene oxide photodetectors by Ag nanoparticles. In 2017 Eleventh International Conference on Sensing Technology (ICST), p. 1–4. https://doi.org/10.1109/ICSensT.2017.8304481

Manzano A, López-Naranjo EJ, Soboyejo W, Meas-Vong Y, Vilquin B. 2015. A review on the efficiency of graphene-based BHJ organic solar cells. J Nanomater. 2015:1–15. https://doi.org/10.1155/2015/406597

Mime FI, Islam MR, Hossain E, Mehedi IM, Hasan MT. 2021. Design and performance analysis of tandem organic solar cells: effect of cell parameter. IEEE Access. 9:40665–40680. https://doi.org/10.1109/ACCESS.2021.3063810

Nguyen DCT, Mai V-D, Tran V-H, Vu V-P, Lee S-H. 2022. Use of modified PEDOT: PSS/Graphene oxide dispersions as a hole transport layer for inverted bulk-heterojunction organic solar cells. Org. Electron. 100:106388. https://doi.org/10.1016/j.orgel.2021.106388

Ohib R, Arnob SY, Ali MS, Sagor RH, Amin MR. n.d. Metal nanoparticle enhanced light absorption in GaAs thin-film solar cell. In 2016 IEEE Asia-Pacific Conference on Applied Electromagnetics, APACE 2016, 2016, p. 89–93. https://doi.org/10.1109/APACE.2016.7916482

Pan S, Liu X, Wang X. 2011. Preparation of Ag2S-graphene nanocomposite from a single source precursor and its surface-enhanced Raman scattering and photoluminescent activity. Mater Charact. 62(11):1094–1101. https://doi.org/10.1016/j.matchar.2011.08.004

Perrozzi F, Prezioso S, Ottaviano L. 2015. Graphene oxide: from fundamentals to applications. J Phys Condens Matter. 27(1):013002. https://doi.org/10.1088/0953-8984/27/1/013002

Ray B, Alam MA. 2012. Achieving fill factor above 80% in organic solar cells by charged interface. In 2012 IEEE 38th Photovoltaic Specialists Conference (PVSC) PART 2, p. 1–8. https://doi.org/10.1109/PVSC-Vol2.2012.6656773

Rivera-Taco J et al. 2021. The role of silver nanoparticles in the hole transport layer in organic solar cells based on PBDB-T: ITIC. J Elec Materi. 50(7):4118–4127. https://doi.org/10.1007/s11664-021-08919-3

Ryu BD et al. 2023. Concurrent thermal reduction and boron-doped graphene oxide by metal–organic chemical vapor deposition for ultraviolet sensing application. Appl Nano. 5(1):1–13. https://doi.org/10.3390/applnano5010001

Sadovnikov SI, Gusev AI. 2017. Recent progress in nanostructured silver sulfide: from synthesis and nonstoichiometry to properties. J Mater Chem A. 5(34):17676–17704. https://doi.org/10.1039/C7TA04949H

Sharma N et al. 2017. Synthesis and characterization of graphene oxide (GO) and reduced graphene oxide (rGO) for gas sensing application. Macromol Symp. 376(1):1–5. https://doi.org/10.1002/masy.201700006

Smith AT, LaChance AM, Zeng S, Liu B, Sun L. 2019. Synthesis, properties, and applications of graphene oxide/reduced graphene oxide and their nanocomposites. Nano Mater Sci. 1(1):31–47. https://doi.org/10.1016/j.nanoms.2019.02.004

Smith CT et al. 2014. Graphene oxide hole transport layers for large area, high efficiency organic solar cells. Appl Phys Lett. 105(7):1–6. https://doi.org/10.1063/1.4893787

Sun F, Ghosh H, Wang J, Tan Z, Sivoththaman S. 2022. A two-step process for reduced graphene oxide films with work function tunability. IEEE Trans Nanotech. 21:481–488. https://doi.org/10.1109/TNANO.2022.3193075

Tran HV et al. 2020. Silver nanoparticles-decorated reduced graphene oxide: a novel peroxidase-like activity nanomaterial for development of a colorimetric glucose biosensor. Arab J Chem. 13(7):6084–6091. https://doi.org/10.1016/j.arabjc.2020.05.008

Vi T et al. 2018. The preparation of graphene oxide-silver nanocomposites: the effect of silver loads on gram-positive and gram-negative antibacterial activities. Nanomaterials. 8(3):163. https://doi.org/10.3390/nano8030163

Wang J et al. 2022. Flexible thermoelectric reduced graphene oxide/Ag2S/methyl cellulose composite film prepared by screen printing process. Polymers (Basel). 14(24):5437. https://doi.org/10.3390/polym14245437

Wiegers. 1971. The crystal structure of the low-temperature form of silver selenide. Am Mineral. 56:1882–1888.